Elastographic versus x-ray CT imaging of radio frequency ablation coagulations: An *in vitro* study

Wu Liu
Department of Medical Physics, University of Wisconsin—Madison, 1300 University Avenue, 1530 MSC, Madison, Wisconsin 53706

Udomchai Techavipoo
Departments of Medical Physics and Electrical and Computer Engineering, University of Wisconsin—Madison, 1300 University Avenue, 1530 MSC, Madison, Wisconsin 53706

Tomy Varghese
Departments of Medical Physics and Biomedical Engineering, University of Wisconsin—Madison, 1300 University Avenue, 1530 MSC, Madison, Wisconsin 53706

James A. Zagzebski and Quan Chen
Department of Medical Physics, University of Wisconsin—Madison, 1300 University Avenue, 1530 MSC, Madison, Wisconsin 53706

Fred T. Lee, Jr.
Department of Radiology, University of Wisconsin—Madison, 1300 University Avenue, 1530 MSC, Madison, Wisconsin 53706

(Received 12 December 2003; revised 20 February 2004; accepted for publication 22 March 2004; published 12 May 2004)

Techniques to image elasticity parameters (i.e., elastography) have recently become of great interest to researchers. In this paper we use conventional ultrasound elastography and x-ray CT to image radio frequency (RF) ablation sites of excised canine liver enclosed in gelatin. Thermal coagulations of different sizes were produced by applying the RF procedure for various times and end point temperatures. Dimensions, areas and volumes computed from CT and elastography were compared with those on whole mount pathology specimens. Ultrasound elastography exhibited high contrast for the thermal coagulations and performed better than CT. The correlation between pathology and elastography for this sample set of 40 thermal coagulations ($r=0.94$ for volume estimation, $r=0.87$ for area estimation) is better than the correlation between pathology and CT ($r=0.89$ for volume estimation, $r=0.82$ for area estimation). © *2004 American Association of Physicists in Medicine.* [DOI: 10.1118/1.1738963]

Key words: CT, elastography, elasticity, image analysis, image-guided therapy, radiofrequency, RF ablation, thermal ablation, strain, ultrasound

I. INTRODUCTION

Although surgical resection is the gold standard for the treatment of most malignant tumors, minimally invasive treatment options are currently available for patients who are technically not eligible for surgical resection or anesthesia, or who refuse surgical intervention. Image-guided tumor ablation has provided an effective and safe means to treat a large variety of benign and malignant conditions and holds promise as a treatment on an outpatient basis.[1–3] The goal for tumor ablation is complete destruction of tumor targets either chemically or thermally using radiofrequency, laser, microwave, high-intensity ultrasound, or cryoablation, without excessive damage to surrounding normal tissue.

Radio frequency (RF) ablation is emerging as a viable modality for many treatment sites. RF ablation is an interstitial focal ablative therapy in which an electrode is placed into a tumor to cause heating and cauterization of the tumor from ionic agitation. The rapid vibration of ions creates friction, and therefore, heating in the region of interest. Insertion of multi-tined, expandable electrodes is a common method for increasing energy deposition and creating a zone of coagulation necrosis of predictable volume.[2,4] RF ablation has the advantages of tissue coagulation at the electrode insertion site (resulting in a low rate of intra- and postprocedural bleeding), percutaneous application via a relatively small electrode,[5,6] and usually a single session of ablation.

The extent of thermal damage depends on the temperature achieved, the duration of application, and the size of the electrode. Mild elevation of the temperature to 40 °C does not destroy the cellular homeostasis, while temperatures greater than 42 °C are considered potentially lethal.[7] Irreversible protein coagulation and cell membrane fusion occurs at a temperature of 46 °C when held for 60 min,[8] while a 4–6 min duration is enough to cause damage at a temperature of 50–52 °C, and cell death happens nearly instantaneously for temperatures over 60 °C.[9] When the temperature reaches 100–105 °C, tissue vaporization, cavitation, and carbonization occur (where the resultant decrease in energy transmission retards ablation[10]). Gas bubbles formed from water vaporization may also destroy cells explosively.[11] Goldberg *et al.*[2] reported that maintaining a 50–100 °C temperature range over the entire target volume is a key for successful ablation.

Imaging modalities that dynamically monitor the irreversible cellular damage evolution during and after treatment are important to the success of rf ablation therapy.[2,3] Ultrasound (US) is a commonly used modality for guidance of rf ablation procedures for hepatic tumors.[2,12] It provides real-time visualization of electrode placement, is portable and cost effective, and can target and guide ablation therapy for most intracavitary and endoluminal applications. Although good correlation between the sizes of sonographically depicted coagulations and pathologic results was reported in earlier literature,[13,14] later reports showed insufficient correlations between pathology and standard B-mode images because of low intrinsic contrast between normal and ablated liver and artifacts from gas bubble formation.[15–17] Dissolved gases (primarily nitrogen) released from cells during heating form gas-bubbles within the tissue, which appear hyperechoic on US images. However, this hyperechoic region does not accurately represent the region of damaged tissue,[15] underestimating the extent of coagulation. In addition, this hyperechoic region fades with time due to the resorption of the gas bubbles.[2,18] US microbubble contrast agents, which help differentiate between perfused and nonperfused tissue, may also be useful in the detection of residual or viable nonablated tumor regions after ablation,[19] but these are still in their infancy.

Magnetic resonance (MR) imaging generally provides excellent tumor-to-tissue contrast for tumor targeting.[2,20] For assessment of the treatment response, the regions of coagulation can be visualized on IV gadolinium contrast enhanced T1- and T2-weighted images because they are devoid of gadolinium enhancement.[21] Another potential advantage of MR-guidance is real-time temperature monitoring during the procedure.[22] Widespread use of MR-guidance for RF ablation is limited because it is expensive, and it requires specialized ablation equipment compatible with high magnetic fields, and precludes patients with metal debris or devices sensitive to these fields. Only one manufacturer currently produces MR compatible RF ablation equipment, with the procedure requiring open MRI.

Recently, combinations of US and computed tomography (CT) or CT alone have been used to optimize RF electrode positioning and coagulated tissue monitoring.[23,24] Ablation procedures were performed under CT guidance, mainly for lesions that are suboptimally visualized using US. Unenhanced CT may be used for targeting and monitoring during the procedure, and contrast enhanced CT may be performed immediately after ablation for treatment assessment. Initial unenhanced CT scans show hypoattenuating RF induced tissue coagulations with variable increased density regions at the center and occasionally a surrounding higher attenuation rim.[2,24–26] The pathological coagulation size closely correlated with the nonenhancing, low-attenuation CT lesion,[13,25–28] e.g., Cha *et al.*[25] showed unenhanced CT and contrast-enhanced CT had better correlation to pathologic size ($r=0.74$ and 0.72, respectively) than US ($r=0.56$). Successful ablation is indicated by low enhancement of the treated area [e.g., less than 10 Hounsfield units (HU)] on the portovenous phase of contrast enhanced CT scans, thus a lack of perfusion in the coagulation.[29] Real-time CT-guidance also has some drawbacks, including repeated exposure to ionizing radiation for both the patient and interventionalist, allergic reactions to iodinated contrast agents, and the amount of contrast agent that can be used (to avoid renal failure) limits the number of scans that can be performed. In addition these procedures typically take up to 3 h, thereby increasing the cost associated with the procedure.[30]

RF ablation is known to cause increases in the stiffness of tissue at the treated site. It is hypothesized that heat-induced protein denaturation by thermal ablative therapy increases randomness of tissue organization, thus the entropy, hence elevation of the elastic modulus of soft tissue.[31] The above results suggest the use of techniques that image tissue stiffness or elasticity variations to monitor and evaluate ablative tissue necrosis.

Several investigators are developing ultrasound techniques for elasticity imaging. Tissue elasticity imaging methods based on US fall into three main groups: (1) methods, that include elastography,[32,33] where a quasi-static compression is applied and the resulting components of the strain tensor estimated,[32–34] (2) methods where a low frequency vibration is applied, with US Doppler detection of velocities of perturbed reflectors,[35–37] and (3) methods that use acoustic radiation force.[38,39]

Elastography[32,33] detects and images the local strain corresponding to small, externally applied quasi-static compression. Local tissue displacements are estimated using a normalized time-domain cross-correlation between gated pre- and postcompression US radio frequency echo signals. The gradient of the tissue displacement in the axial direction provides an estimate of local tissue strain. Although elasticity data are generally obtained using offline processing, several groups have shown real-time application of elastography using faster algorithms[40] or by implementing the algorithms on clinical scanners.[41]

Elastography is sensitive to small changes in elastic modulus,[42] and, thus, it has the potential to image and differentiate the thermal coagulation necrosis from normal surrounding tissues. *In vitro* and preliminary *in vivo* studies have demonstrated the feasibility of elastography for monitoring the impact of tumor ablation using laser[43] and high-intensity focused US (HIFU).[44–46] Our preliminary *in vivo* animal results[47] illustrate that boundaries between RF-induced coagulations and normal liver on elastographic images are shown much better than those on sonography. Elastography may therefore provide substantial improvements over sonography in the ability to monitor RF ablation coagulations in clinical use. 3D visualization of thermal coagulations by elastography[48] revealed high coagulation-to-tissue contrast and good correlation with pathology.

The purpose of this study was to compare the *in vitro* performance of elastography with x-ray CT, the current preferred imaging modality for RF ablation monitoring and evaluation. The appearance of the coagulated necrotic region on elastography and CT images and the correlation among elastographic, CT, and pathological measurements of coagulation area and volume are evaluated and compared. Elastog-

raphy may replace the relatively high cost and contrast required modality in the future if the elastographic performance is comparable with that of x-ray CT in clinical situations. In this paper, we compare the *in vitro* thermal coagulation delineation performance of CT without contrast with elastography on the same coagulations. These comparisons were performed since previous literature results have reported good depiction of the coagulated boundaries with unenhanced CT.[25] For *in vivo* evaluation of the elastographic depiction of coagulations, comparison with x-ray CT will be important both with and without contrast, and will be performed as part of future studies.

II. MATERIAL AND METHODS

RF ablation *in vitro* was performed on specimens of freshly excised canine liver tissue having approximate dimensions of 40 mm by 30 mm, and 25–40 mm thickness. A RITA model 1500 RF generator (RITA Medical System, Mountain View, CA) with nine StarBurst XL multitined expandable electrodes was used for the ablation procedures. This generator delivers 460 kHz electromagnetic waves. The electrode consists of a 15 cm long 14 gauge stainless steel shaft insulated to within 1 cm of the tip by a thin plastic layer, through which nine sharp tines (0.53 mm in diameter) can be deployed or retracted manually. The last 1 cm of the tip and each tine constitute the electrically active surface. The electrode was inserted into a liver specimen, and the tines were carefully deployed to provide 2–3 cm active lengths in addition to the 1 cm active tip of the shaft. The tines are deployed in an ''umbrella'' configuration at 45 degree intervals, along with the central tine. A foil ground pad was attached to the bottom surface of the liver specimen. RF ablation of the target tissue was performed at a 150 W power level for 1, 2, 5, or 10 min durations after the target temperature (90 °C) was reached to create coagulations with different sized volumes. The electrode has five independent thermocouples incorporated into the tines, providing real-time temperature feedback to maintain an average of the five temperatures at 90 °C, thereby preventing both insufficient and excessive heating. In our experiments, the temperatures on individual tines were in the range of 80–105 °C. The system also measures tissue impedances, which were on the order of 80 to 40 ohms, with decreasing values during ablation. We chose regions located in liver parenchyma away from the porta hepatis, large vessels, and visualized fissures to create thermal coagulations. Although we attempted to create coagulations away from the liver surface, several large coagulations created by 5 or 10 min ablations extended to the surface, resulting in a bell-shaped lesion instead of the desired ellipsoid cross section. Forty RF coagulations were created, scanned, and measured to obtain the thermal coagulation area and volume.

Gelatin phantoms

After the ablated liver specimen had cooled to room temperature, it (along with the RF electrode, for inscribing fiducial markers) was encased in a gelatin block, 110 mm by 80 mm and 70 mm thick, for subsequent imaging. Gelatin phantoms were prepared using 200-bloom calfskin gel at a concentration of 15.4 g per liter of distilled water. The gelatin powder was mixed with distilled water and cooked in a double-heated water bath to a temperature of 80 °C. After the gelatin solution clarified, glass beads with a mean diameter of 18 μm were added at a concentration of 1 g of beads/liter of molten gelatin. The beads are a source of scattered echo signals during sonographic imaging. The glass beads were mixed with warm distilled water and stirred carefully into the molten gelatin. Molten gelatin was then poured into plexiglass molds. First a layer of molten gelatin about 2.5 cm thick was poured at a temperature of 29 °C. After this layer congealed, a lobe of liver with its RF ablation coagulation was placed on this gelatin layer. The mold was then filled with molten gel at 29 °C, and the entire phantom was allowed to congeal for an hour. The molds containing the gelatin blocks were then refrigerated at 10 °C to solidify overnight.

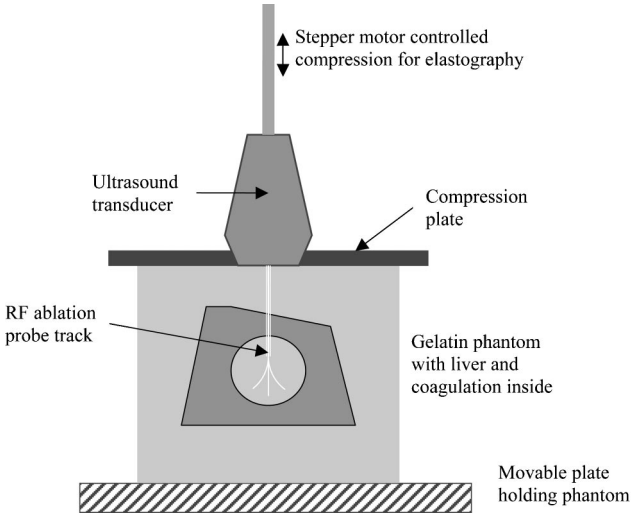

FIG. 1. Experimental setup used for radiofrequency ablation elastography.

Elastographic imaging

On the second day after the procedure, the gelatin block containing liver specimen was removed from the mold and placed in an apparatus for elastographic imaging (Fig. 1) at room temperature. An Aloka SSD 2000 (Aloka, Tokyo, Japan) real-time ultrasound scanner with a 42 mm 5-MHz linear array transducer with a 70% bandwidth was used. The use of a transducer with a large bandwidth and high center frequency improves the signal-to-noise ratio on elastograms.[49] The apparatus includes a compression plate, controlled by a stepper motor to achieve precise compressions of the gelatin block. The plate is larger than the surface of the phantom to maintain a uniform applied axial stress distribution. The plate is in direct contact with the gelatin block during data acquisition. The transducer was mounted into the compression plate and acoustically coupled to the gelatin phantom through a slot. The compression and data acquisition operation are controlled by a personal computer.

A total of five compression steps for each scanning plane were acquired using compressive increments of 0.5% (0.35 mm displacement), for a total of six US RF frames and a 2.5% maximum compression. The raw US RF echo signals from each B-mode frame (4096 points—63 mm along the longitudinal axis, 220 A-lines—40 mm along the transverse axis) were digitized using a 12-bit data acquisition board (Gage Applied Inc, Lachine, QC, Canada) at a sampling rate of 50 MHz for offline processing. Beam lines were parallel to the ablative electrode track after the electrode was removed. By manually translating the gelatin block parallel to the scan plane and repeating the data acquisition steps for each plane, 3D elastographic data were acquired. A 2 mm distance between planes (the elevational resolution is slightly larger than 2 mm) was precisely controlled using a precision linear stage.

Elastographic processing

Time-domain cross-correlation analysis of RF echo signals from the pre- and postcompression data sets was performed using a window length of 3 mm with a 75% overlap between data segments to compute tissue displacements. The choice of window length and overlap was a tradeoff between the contrast-to-noise ratio (CNR_e) and the axial resolution.[33] Axial strain was estimated using a least squares strain estimator[50] with a kernel size of 2.25 mm. A 5×1 ($3.75\ \text{mm}\times0.2\ \text{mm}$) median filter was used to remove outliers in the displacement data before strain estimation. The length of this filter is only slightly larger than the window size, hence the probable resolution loss is not significant. Five 0.5% compression elastograms were obtained for each parallel plane from the five 0.5% compressions. In the B-mode images, the sonographic signal-to-noise ratio (SNR_s) was low in regions distal to the coagulation because of shadowing and occasionally from artifacts around the electrode track. These low SNR_s regions in turn result in a low SNR_e in the corresponding parts of the elastogram. A 3×3 ($2.25\ \text{mm}\times0.6\ \text{mm}$) median filter was applied on the strain elastograms to reject noise artifacts. The remaining low SNR_e points were arbitrarily set to a 0.5% strain, and multi-compression averaging[51] was performed on the five 0.5% elastograms. The applied compression reduces the thickness of the gelatin block and liver specimen. Therefore, before averaging, the five elastograms were resized by linear interpolation to correspond to the original dimension. An alpha-trimmed mean filter[52] (trim size$=d/2=1$, maximum and minimum values excluded) was used for point-by-point averages among the five images, where this filter further reduces noise artifacts. A 3×3 ($0.6\ \text{mm}\times0.6\ \text{mm}$) median filter was applied again on the multi-compression averaged elastogram to acquire a smoother image. All the resultant elastograms were displayed on a fixed strain dynamic range scale of 0%–2%.

X-ray CT scans

CT imaging was performed on the same gelatin phantoms within a few days of the elastographic scans using a CTi helical scanner (General Electric Medical Systems, Milwaukee, WI) using 120 kVp, 250 mA, 3 mm collimation. A pitch of 1.4:1 was used to blur the image in the z-dimension to reduce the gap artifacts. Besides 3D scans, a laser light aligned, one-slice scan was performed at the cross-section where the ablative electrode was inserted. The image plane was marked on the gelatin phantom, and it will be referred to in this paper as the ''central plane.''

Pathology

After CT imaging, the gelatin blocks with the liver specimen inside were sliced along the central planes, placed on a transparent film, and photographically scanned (digitized at 300 dpi resolution) to obtain fresh liver/coagulation images for area estimates. The liver specimens were then removed from the gelatin molds, immersed in 10% buffered neutral formalin solution, and allowed to fix for at least 2 weeks. After the tissue was completely fixed, each liver specimen was sliced (by a mechanical tissue slicer) in the axial plane approximating the elastographic imaging planes in 2 mm intervals. The tissue slices were placed on a transparent film and photographically scanned similar to the fresh pathology to obtain fixed pathology images of the same lesion. These fixed gross-pathology images were used to obtain both area and volume estimations of the thermal coagulation.

Area and volume measurements

Coagulation boundaries of each slice were manually delineated on the elastogram, x-ray CT image, and digitally scanned pathology image. Binary images were created, designated by ''1'' inside or on the thermal coagulation boundary and ''0'' outside the coagulated region. The coagulation area for each slice was estimated by summing the number of pixels that represent a binary value of 1, and multiplying the sum of pixels by the area of each pixel. The area of an individual pixel was determined by its 2-by-2 neighborhood. The coagulation volume was similarly computed by summation of the product of the area (as described above) obtained in each slice times the slice thickness. The slice thickness for elastographic measurements was 2 mm, which was controlled by the precision linear stage. The slice thickness of the x-ray CT images was 3 mm, which was controlled by collimation. The slice thickness of pathology was taken as the mean of eight measurements on the same slice using a micrometer caliper.

III. RESULTS

Visualization of RF-induced coagulations

Figure 2 presents matching sonogram, elastogram, CT, and pathology images of a cross-section (along the electrode track) from a typical RF-induced coagulation. All the images are at the same scale, with the images from different modalities registered manually to a common coordinate system. The RF electrode track can be seen on all the images (white arrows), indicating a correct registration of the imaging planes.

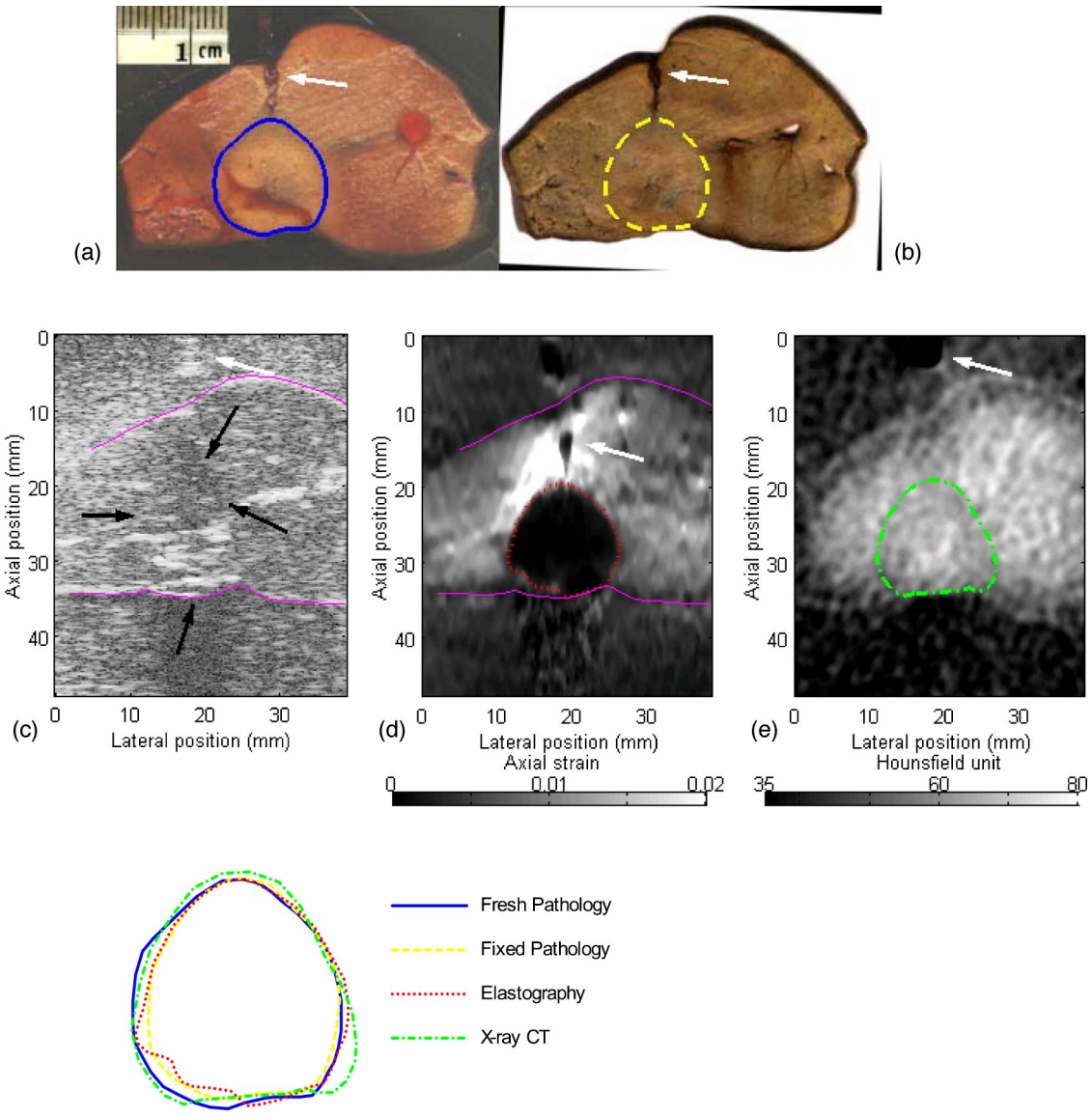

FIG. 2. Typical RF ablation coagulation on freshly excised canine liver. (a) Fresh pathology photograph of the central plane, showing a white area of coagulation necrosis and a darker zone of charring. The solid-line contour is the outer boundary of the white region. (b) Fixed pathology photography of the same liver slice. The dashed-line contour is the outer boundary of the white zone. (c) Linear B-mode gray scale ultrasound image of the same liver slice. Solid curves are the boundary of the liver as defined from the B-mode image. Note that the coagulated region boundary is difficult to delineate. (d) Corresponding elastogram obtained using 0.5% applied compression and displayed using a strain dynamic range of 0 to 2%. Dotted-line contour is the boundary of the coagulated region. (e) Corresponding nonenhanced CT image, displayed at a window level of 58HU and a window width of 45HU, showing a hyperattenuation core and a surrounding hypo-attenuation region at the site of tissue coagulation. Dash-dotted-line contour is the manually drawn liver-coagulation boundary from the outer boundary of the hypo-attenuation zone. The precise edge of the coagulation is somewhat ambiguous. (f) Overlapped contours of the coagulation boundaries as interpreted in (a)–(e).

The pathological photographs were trimmed to 51 mm by 35 mm to show the entire slice of the liver specimen. The contours on the images were drawn manually.

Figure 2(a) displays the fresh pathology photograph of the central plane, cut immediately after the CT scan. It depicts a white, circular area of coagulative necrosis and a darker zone of charring. The solid-line contour was drawn of the outer boundary of the white coagulation region. Most *in vivo* RF-induced lesions contain a central white zone representing coagulation necrosis and a surrounding red ring of about 1–5 mm thickness, representing hemorrhagic and inflammatory reactions.[3,25,53] However, this red zone of hyperemia is usually absent in *ex vivo* specimens.[54] The red zone was not clearly visible on most of our specimens, but we did see a thin transitional zone from the necrotic region to the normal liver tissue in several cases. Figure 2(b) displays the pathology photograph of the same liver slice after fixing with formalin. The dashed-line contour identifies the outer boundary of the white coagulation zone from fixed pathology. Figures 2(c)–2(e) demonstrate that the coagulation-to-liver contrast of the elastogram is much better than that of the other two modalities. The B-mode gray scale US image [Fig. 2(c)] shows both hyperechoic and hypoechoic regions at the place of the apparent coagulation site. Shadowing below the co-

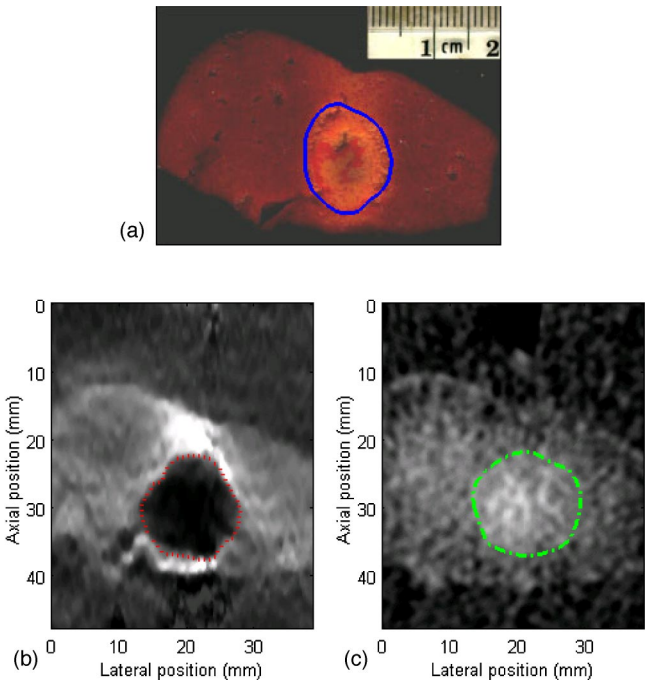

FIG. 3. Another typical RF ablation coagulation to illustrate the reproducibility of our results and the slightly different coagulation visualization of CT. In contrast to the CT image shown in Fig. 2(e), (c) reveals the coagulation as a hyper-attenuation, circular region without a visible surrounding hypo-attenuation zone. As in Fig. 2, the coagulation location and size viewed on the elastogram and CT correlates with that seen on pathology.

agulation region is remarkable, but the coagulation-liver interface is difficult to delineate. However, the liver-gel boundaries, delineated by solid curves, are hyperechoic and better defined than those on the matching elastogram and CT image. An elastogram [Fig. 2(d)] displayed over a strain dynamic range of 0% to 2% reveals the RF-induced coagulation as a stiff (dark) area of very low strain (0.05%). The average strain is 1% in the normal liver area and 0.4% in the gelatin block. The sonographic shadowing with low signal levels distal to the coagulation zone generates an area of corresponding decorrelation noise in the elastogram. The dotted-line contour is the boundary of the coagulation necrosis depicted manually. For this case, the coagulation necrosis touches the surface of the liver, which makes the depiction of the lower coagulation boundary difficult. The liver boundary information provided by the US image is helpful in determining the lower boundary of coagulation on the elastogram for those large thermal coagulations that extend to the surface of the liver. On the CT scan [Fig. 2(e)] displayed at a window level of 58HU and window width of 45HU, the coagulation zone is characterized by a hyper-attenuating core and a surrounding hypo-attenuating region (this is different from the case shown in Fig. 3). The precise edge of the coagulation is ambiguous (the HU contrast between the coagulation and the surrounding normal tissue is only a few HU). The dash-dot contour is a manually delineated CT boundary of the coagulation (outer boundary of the hypo-attenuation zone). Figure 2(f) shows the relative overlap of observer-defined coagulation boundaries traced from the different modalities. They correspond to each other very well. The CT boundary is slightly larger than the pathology one, while the one obtained with elastography is slightly smaller.

In contrast to the case shown in Fig. 2, for the majority of the RF-induced coagulations CT scans reveal the coagulation zone as a hyper-dense region without a visible surrounding hypo-dense zone. A typical coagulation without a visible surrounding hypo-dense zone viewed in fresh pathology, elastography, and CT is shown in Figs. 3(a)–3(c). Note that the coagulation on the elastogram/CT correlates with pathology. As previously described, it is quite difficult to delineate the thermal coagulation from the CT images, where the boundaries are at best ambiguous. The contours on the CT images were drawn based upon knowledge of typical thermal coagulation geometries.

Area and volume correlation analysis

Observer-defined coagulations on elastograms and CT images were compared with pathological specimens for 40 thermal coagulations. To create lesions of different sizes, heating durations of 1, 2, 5, and 10 min were applied, with ten specimens used at each heating duration. Both two-dimensional contours and volumes were estimated from the images. Pathology analysis was performed after elastographic and CT imaging measurements for each specimen to avoid observer's preknowledge of the shape and size of the actual thermal coagulation.

Two experienced ultrasound physicists also examined sonograms of the thermal coagulations along the central plane. The echogenicity of the RF coagulations was variable, with 10 hypoechoic, 2 hyperechoic, 1 isoechoic, and 27 mixed-echoic found by one observer, whereas 10 hypoechoic, 4 hyperechoic, 8 isoechoic, and 18 mixed-echoic were found by the other observer. The discrepancy between observers reflects the subjectivity of the analysis and uncertainties because of the small echogenicity difference between normal liver and damaged tissue. Also, because the electrode track often shows up as hyperechoic, some hypoechoic coagulations were classified as mixed. This is probably one of the reasons that the percentage of hypoechoic lesions (25%) is much lower than the 59% reported by Cha *et al.*[25]

Elastographic estimates of the coagulation area were recorded by manually drawing contours (dotted-line contour on Figs. 2 and 3) of the dark (stiffer) region on the elastograms. Contouring was performed on the same monitor with the same monitor setting and strain dynamic range (0% to 2%) for all elastograms. Manual contouring on CT images also used the same monitor and settings. The window level for CT images was fixed to 58HU and the window width was fixed at 45HU, except for a few cases of higher average HU. The zones of ablation were determined on CT images as the outer boundary of the hypo-dense ring similar to those shown in Fig. 2 (dash-dotted-line contour). For cases similar to the one shown in Fig. 3, the outer boundary of the hyper-dense lesion (dash-dotted-line contour) was depicted. Only the white zone (complete dead tissue) was included for gross pathological examination (solid-line contour on fresh pathol-

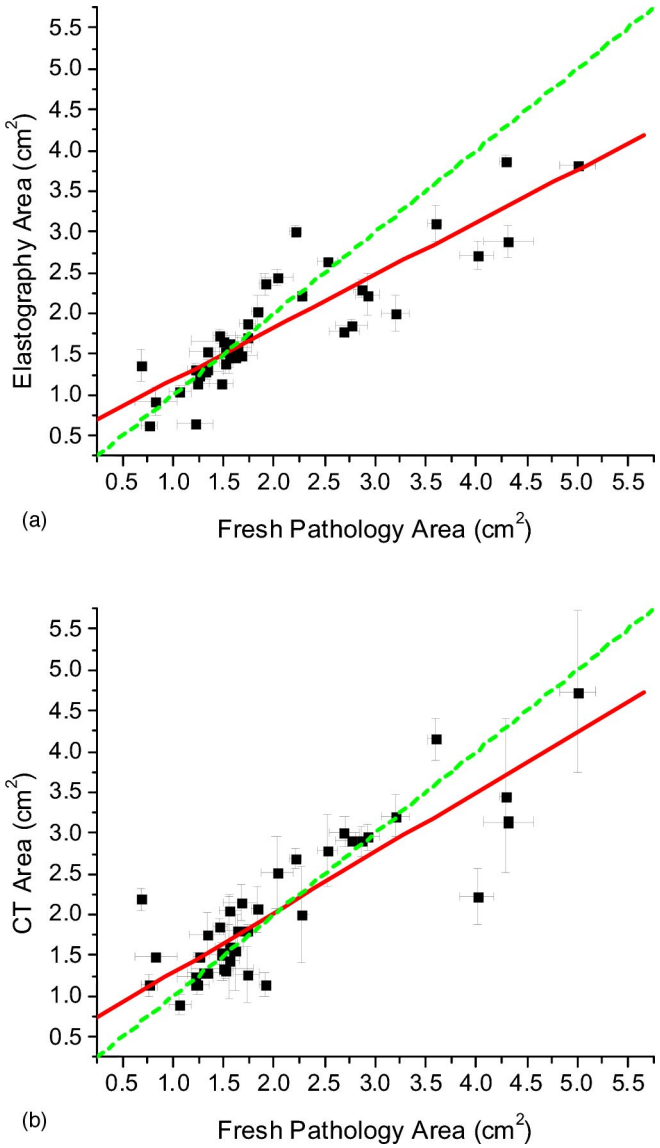

FIG. 4. Scatter plots of coagulation areas comparing (a) areas on elastograms and (b) areas on CT with the area outlined on freshly sliced tissue pathology at the central plane. The solid lines indicate a linear fit of the data from 40 independent samples. The dashed lines are functions of $y=x$, indicating a perfect correlation between elastographic/CT areas and pathology. Error bars are the standard deviation of four measurements by a single observer on each sample, representing the uncertainty of the measurements. The correlation coefficient between elastography and pathology area ($r=0.88$) is slightly better than that between CT and pathology area ($r=0.85$).

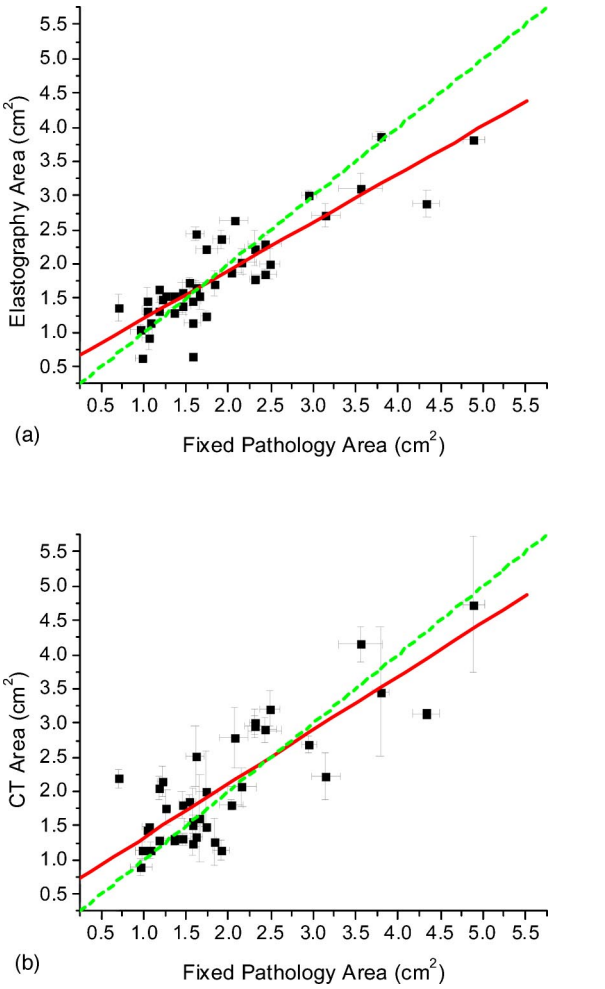

FIG. 5. Scatter plot of coagulation area measurements, comparing (a) elastographic areas and (b) CT areas with areas from fixed tissue pathology for the central planes. The correlation coefficients ($r=0.87$ for elastography and $r=0.82$ for CT) are a little worse than those in Fig. 4, likely due to the shrinkage of the fixed specimen.

ogy and dashed-line contour on fixed pathology in Figs. 2 and 3).

Figure 4 shows scatter plots of ablation areas, comparing elastographic [Fig. 4(a)] and CT areas [Fig. 4(b)] with freshly sliced pathology areas along the central plane. The solid lines indicate the linear fit of the data from 40 independent specimens, while the dashed lines indicate perfect correlation (slope equals 1). Error bars are the standard deviation of four measurements by a single observer on each specimen, representing the uncertainty of the measurements. Generally the error bars of the pathology and elastographic data are smaller than those of the CT data. For example, the average percent standard deviations (SD) over the 40 coagulation area estimates in the central plane for fresh pathology, elastogram, and CT images were 6%, 6%, and 11% respectively. The correlation coefficient between elastography and pathology areas ($r=0.88$) is better than between CT and pathology area ($r=0.85$). Figure 5 shows scatter plots of ablation area measurements comparing elastographic areas or CT areas with the fixed tissue pathology at the central planes. The correlation coefficients ($r=0.87$ for elastography and $r=0.82$ for CT) are a little worse than those presented in Fig. 4. This is probably because after fixation, the liver specimen deforms and shrinks to some extent, making the correlation worse. However, because the coagulation is much stiffer than normal liver tissue, we believe that it shrunk less than liver tissue. Figure 6 shows that the areas on fixed pathology specimens are in general a few percent smaller than those from fresh pathology.

Figure 7 displays scatter plots of coagulation volume measurements comparing elastographic volumes or CT volumes with the fixed tissue pathology. The correlation coeffi-

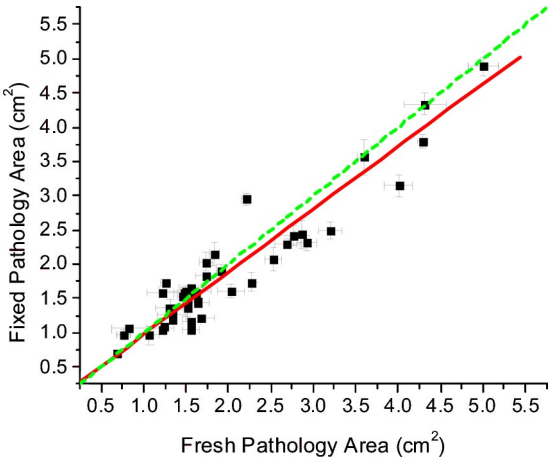

FIG. 6. Coagulation areas measured on fixed versus fresh pathological samples. The fixed pathology areas are a few percent smaller than those on fresh pathology, probably due to specimen shrinkage in formalin solution.

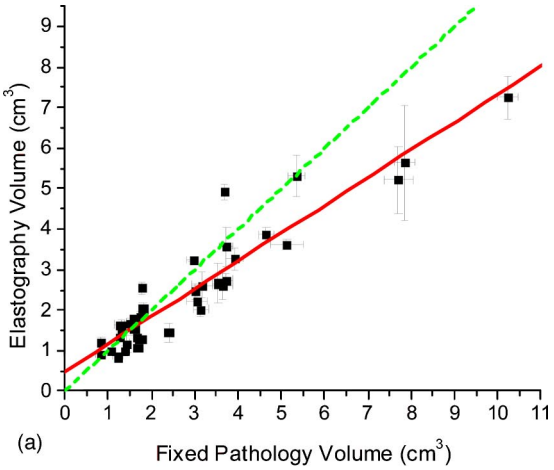

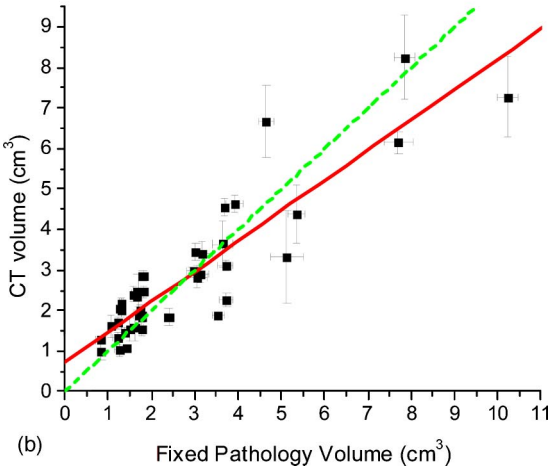

FIG. 7. Scatter plots of coagulation volume measurements comparing (a) elastographic volumes and (b) CT volumes with volumes computed for fixed tissue pathology specimens. The correlation coefficient between volumes depicted on elastography and those on pathology ($r=0.94$) is slightly better than that between CT and pathology ($r=0.89$).

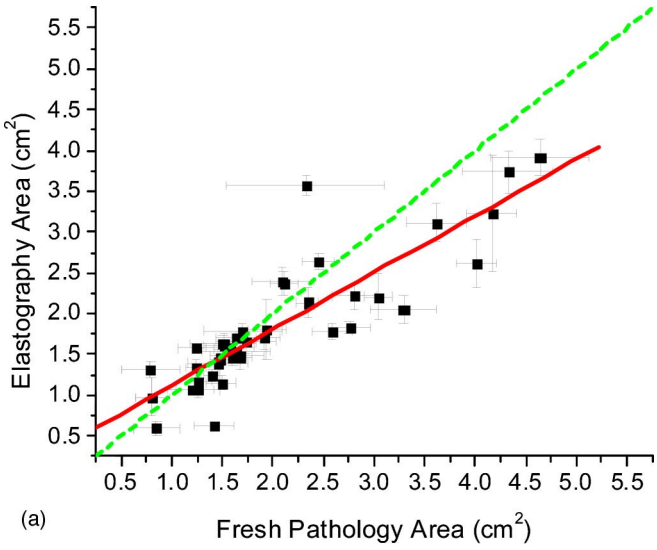

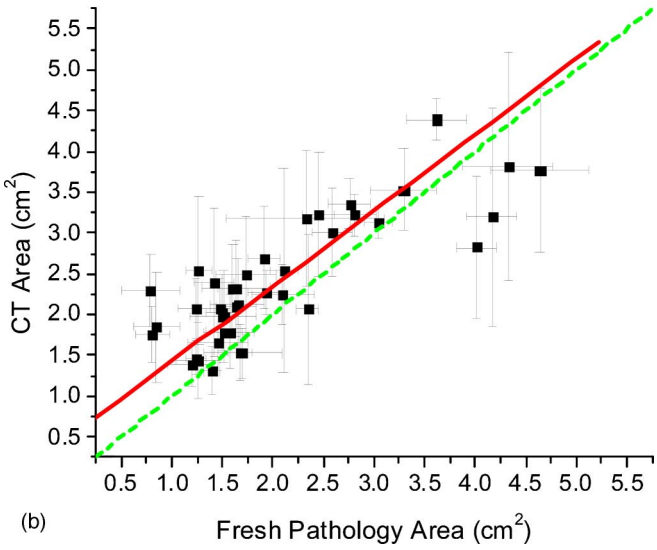

FIG. 8. Multi-observer study of manual area delineation of thermal coagulations obtained using (a) elastograms and (b) x-ray CT images. Comparisons were performed along the central plane of the thermal coagulation, with the x-axis in both plots denoting the pathology areas of fresh tissue ($r=0.87$ for elastography and $r=0.82$ for CT). The error bars denote the variation in the results obtained from the five independent observers. Note the error bars of CT results are much larger than those of elastographic results.

cient between elastography and pathology volume is $r=0.94$ and between CT and pathology volume is $r=0.89$. Elastography tends to slightly underestimate the actual coagulation size found on gross pathology.

Multiobserver analysis was performed over thermal coagulation data sets that included x-ray CT and elastographic images. The results are shown in Fig. 8. Five independent observers blinded to the other data sets manually delineated the thermal coagulation boundaries for the central slices of all 40 lesions. The mean values obtained are represented as square data points, while the error bars denote the standard deviation among observer results. Note, from Fig. 8, that the

TABLE I. Imaging-pathology correlations on coagulation area and volume.

Imaging modality	Correlation with pathology (fresh for area, fixed for volume)		
	$r1_{area}$ [a]	$r1_{volume}$ [b]	$r2_{area}$ [c]
Elastography	0.88	0.94	0.87
X-ray CT	0.85	0.89	0.82

[a]Correlation coefficient of coagulation area (single observer analysis).
[b]Correlation coefficient of coagulation volume (single observer analysis).
[c]Correlation coefficient of coagulation area (multi-observer analysis).

r-value for the correlation between the mean area estimates obtained with elastography and pathology is 0.87 while that between CT and pathology is 0.82. However, the more significant aspects are the large error bars in the CT area estimates [Fig. 8(b)] among the five observers. These are significantly greater than those obtained for the elastography estimates [Fig. 8(a)]. Another point to be made is that only one of the area estimates in Fig. 8(a) out of 40 estimates has a standard deviation similar to CT estimates. Almost all of the CT estimates exhibit large error bars. The results in Fig. 8 demonstrate the reproducibility of elastographic area estimates for delineating thermal coagulations. Table I is a summary of our correlation measurements.

IV. DISCUSSION

Imaging modalities which can monitor the irreversible cellular damage evolution during and after treatment are important to the success of RF ablation.[2,3,55] It is generally recognized that tissue-coagulation interfaces are better visualized with CT or MRI than conventional sonography. Radiological and pathological correlations in both experimental and clinical studies have shown that CT and MRimaging predict the region of coagulation to within 2–3 mm with good correlation to pathology.

In this study we demonstrate good correlation between elastographic and gross pathological coagulation areas ($r=0.88$) and volumes ($r=0.94$). Correlations between measures from elastogram and pathology were better than those between unenhanced CT and pathological measurements ($r=0.86$ for area and $r=0.90$ for volume). This is due to the large stiffness contrast between the zone of ablation and the surrounding normal tissue (coagulations are about an order of magnitude stiffer than normal tissue), whereas on CT images the margins of the ablation zone are often diffuse and the HU difference between ablation and normal tissue are often low (5–25HU). The HU density of normal liver and thermal coagulation varies from specimen to specimen. For liver values ranged from 35 to 60HU, and for thermal coagulations the values were between 50 and 80HU. This also explains the fact that the error bars on the CT versus pathology area and volume plots are generally larger than those on the elastography versus pathology plots. The correlations between imaging modality and pathology for volume data are better than those for area data for both elastography and CT. This is because area measurements are sensitive to registration between the pathology slice and the scan plane, whereas volume measurements are less sensitive to this error. Due to the significant changes in the shape of small thermal coagulations, slight differences in imaging plane on sonography or CT could substantially change the area estimates of the coagulation zone. This is also probably one of the reasons that our result for CT is better than that reported by Cha *et al.*,[25] since they only measured the 1D size of the ablative zone. However, the high correlations ($r=0.93-0.95$) reported by Raman *et al.*[26] on CT measurements might be because they only analyze spherical or oval lesions without any contour distortion caused by major vessels, the liver surface, or interlobar fissures.

Stafford *et al.*[43] reported an $r=0.85-0.92$ correlation between elastographic and pathological 1D size measurement of laser-induced thermal coagulation, while Righetti *et al.*[45] reported an $r=0.96$ correlation between pathology and elastography for area measurements of HIFU-induced thermal coagulation. Our earlier study[48] showed an $r=0.87$ on size, $r=0.94$ on area and 0.98 for volume measurement of RF-induced thermal coagulation. Results in this paper show a slightly lower correlation due to the low SNR along the RF electrode track. In contrast to our early study,[48] where we scanned the specimen perpendicular to the RF electrode, we did the US scans parallel to the RF electrode in the present study. This arrangement also makes the measurements more difficult because the shape of the ablative zones on these planes are not as regular as those on planes perpendicular to the RF electrode. For those coagulations that extended to the distal surface of the liver, shadowing often made it difficult to demarcate the distal boundary of the coagulation on the elastogram.

Clear delineation of the coagulation on CT scans requires intravenous injection of contrast agent, where the coagulation does not enhance because of vascular obliteration. Because contrast enhancement is required to clearly identify the coagulation, CT might not be a preferred means for continuous monitoring of the coagulation development during treatment. However, elastography provides another option for monitoring RF ablation procedures.

In this paper we demonstrate that elastography is a promising clinical tool for monitoring and assessing the success of the therapy immediately after RF ablation. In previous work, we have shown feasibility for *in vivo* elastographic imaging where the RF electrode is used as a compressor.[47] The use of the RF ablation electrode as the compression/displacement device reduces lateral slippage or nonaxial motion that may occur with externally applied compressions or imaging during the respiratory cycle.

V. CONCLUSION

The high correlation between elastographic and pathological measures of coagulation created by RF ablation, as well as the fact that elastography offers a real-time imaging capability, implies that this modality could be superior to unenhanced x-ray CT as well as conventional B-mode US for guiding and monitoring RF ablative therapy in soft tissue sites.

ACKNOWLEDGMENTS

The authors thank Gary Frank, Larry Whitesell, Jennifer Buck, and Carrie Murphy for providing support for the experiments. This work was supported in part by Whitaker Foundation Grant No. RG-02-0457, start-up funds awarded to Dr. Varghese by the University of Wisconsin—Madison, and by NIH Grant No. R21-EB002722.

[1] J. T. De Sanctis, S. N. Goldberg, and P. R. Mueller, ''Percutaneous treatment of hepatic neoplasms: A review of current techniques,'' Cardiovasc. Intervent Radiol. **21**, 273–296 (1998).
[2] S. N. Goldberg, G. S. Gazelle, and P. R. Mueller, ''Thermal ablation therapy for focal malignancy: a unified approach to underlying principles, techniques, and diagnostic imaging guidance,'' AJR, Am. J. Roentgenol. **174**, 323–331 (2000).
[3] S. N. Goldberg, J. W. Charboneau, G. D. Dodd III, D. E. Dupuy, D. A. Gervais, A. R. Gillams, R. A. Kane, F. T. Lee, Jr., T. Livraghi, J. P. McGahan, H. Rhim, S. G. Silverman, L. Solbiati, T. J. Vogl, and B. J. Wood, ''Image-guided tumor ablation: proposal for standardization of terms and reporting criteria,'' Radiology **228**, 335–345 (2003).
[4] S. Rossi, E. Buscarini, F. Garbagnati, M. Di Stasi, P. Quaretti, M. Rago, A. Zangrandi, S. Andreola, D. Silverman, and L. Buscarini, ''Percutaneous treatment of small hepatic tumors by an expandable RF needle electrode,'' AJR, Am. J. Roentgenol. **170**, 1015–1022 (1998).
[5] H. Rhim and G. D. Dodd III, ''Radiofrequency thermal ablation of liver tumors,'' J. Clin. Ultrasound **27**, 221–229 (1999).
[6] T. Livraghi, S. N. Goldberg, S. Lazzaroni, F. Meloni, L. Solbiati, and G. S. Gazelle, ''Small hepatocellular carcinoma: treatment with radiofrequency ablation versus ethanol injection,'' Radiology **210**, 655–661 (1999).
[7] G. L. Rosner, S. T. Clegg, D. M. Prescott, and M. W. Dewhirst, ''Estimation of cell survival in tumours heated to nonuniform temperature distributions,'' Int. J. Hyperthermia **12**, 223–239 (1996).
[8] T. R. Larson, D. G. Bostwick, and A. Corica, ''Temperature-correlated histopathologic changes following microwave thermoablation of obstructive tissue in patients with benign prostatic hyperplasia,'' Urology **47**, 463–469 (1996).
[9] S. N. Goldberg, L. Solbiati, G. S. Gazelle, K. K. Tanabe, C. C. Compton, and P. R. Mueller, ''Treatment of intrahepatic malignancy with radiofrequency ablation: radiologic-pathologic correlation in 16 patients (abstr). [American Roentgen Ray Society 97th Annual Meeting Program Book suppl],'' AJR, Am. J. Roentgenol. **168**, 121 (1997).
[10] S. N. Goldberg, G. S. Gazelle, E. F. Halpern, W. J. Rittman, P. R. Mueller, and D. I. Rosenthal, ''Radiofrequency tissue ablation: importance of local temperature along the electrode tip exposure in determining lesion shape and size,'' Acad. Radiol. **3**, 212–218 (1996).
[11] A. L. McKenzie, ''Physics of thermal processes in laser-tissue interaction,'' Phys. Med. Biol. **35**, 1175–1209 (1990).
[12] A. Giorgio, L. Tarantino, G. de Stefano, V. Scala, G. Liorre, F. Scarano, A. Perrotta, N. Farella, V. Aloisio, N. Mariniello, C. Coppola, G. Francica, and G. Ferraioli, ''Percutaneous sonographically guided saline-enhanced radiofrequency ablation of hepatocellular carcinoma,'' AJR, Am. J. Roentgenol. **181**, 479–484 (2003).
[13] R. Yang, K. K. Kopecky, F. J. Rescorla, C. A. Galliani, E. X. Wu, and J. L. Grosfeld, ''Sonographic and computed tomography characteristics of liver ablation lesions induced by high-intensity focused ultrasound,'' Invest. Radiol. **28**, 796–801 (1993).
[14] S. A. Curley, B. S. Davidson, R. Y. Fleming, F. Izzo, L. C. Stephens, P. Tinkey, and D. Cromeens, ''Laparoscopically guided bipolar radiofrequency ablation of areas of porcine liver,'' Surg. Endosc **11**, 729–733 (1997).
[15] D. E. Malone, L. Lesiuk, A. P. Brady, D. R. Wyman, and B. C. Wilson, ''Hepatic interstitial laser photocoagulation: demonstration and possible clinical importance of intravascular gas,'' Radiology **193**, 233–237 (1994).
[16] L. Solbiati, S. N. Goldberg, T. Ierace, T. Livraghi, F. Meloni, M. Dellanoce, S. Sironi, and G. S. Gazelle, ''Hepatic metastases: percutaneous radio-frequency ablation with cooled-tip electrodes,'' Radiology **205**, 367–373 (1997).
[17] J. R. Leyendecker, G. D. Dodd III, G. A. Halff, V. A. McCoy, D. H. Napier, L. G. Hubbard, K. N. Chintapalli, S. Chopra, W. K. Washburn, R. M. Esterl, F. G. Cigarroa, R. E. Kohlmeier, and F. E. Sharkey, ''Sonographically observed echogenic response during intraoperative radiofrequency ablation of cirrhotic livers: pathologic correlation,'' AJR, Am. J. Roentgenol. **178**, 1147–1151 (2002).
[18] N. A. Watkin, G. R. Ter Haar, S. B. Morris, and C. R. Woodhouse, ''The urological applications of focused ultrasound surgery,'' Br. J. Urol. **75** (Suppl 1), 1–8 (1995).
[19] L. Solbiati, M. Tonolini, L. Cova, and S. N. Goldberg, ''The role of contrast-enhanced ultrasound in the detection of focal liver lesions,'' Eur. Radiol. **11** (Suppl 3), E15–26 (2001).
[20] E. M. Merkle, J. R. Shonk, L. Zheng, J. L. Duerk, and J. S. Lewin, ''MR imaging-guided radiofrequency thermal ablation in the porcine brain at 0.2 T,'' Eur. Radiol. **11**, 884–892 (2001).
[21] T. L. Boaz, J. S. Lewin, Y. C. Chung, J. L. Duerk, M. E. Clampitt, and J. R. Haaga, ''MR monitoring of MR-guided radiofrequency thermal ablation of normal liver in an animal model,'' J. Magn. Reson Imaging **8**, 64–69 (1998).
[22] B. Quesson, J. A. de Zwart, and C. T. Moonen, ''Magnetic resonance temperature imaging for guidance of thermotherapy,'' J. Magn. Reson Imaging **12**, 525–533 (2000).
[23] W. W. Mayo-Smith, D. E. Dupuy, P. M. Parikh, J. A. Pezzullo, and J. J. Cronan, ''Imaging-guided percutaneous radiofrequency ablation of solid renal masses: techniques and outcomes of 38 treatment sessions in 32 consecutive patients,'' AJR, Am. J. Roentgenol. **180**, 1503–1508 (2003).
[24] M. A. Farrell, W. J. Charboneau, D. S. DiMarco, G. K. Chow, H. Zincke, M. R. Callstrom, B. D. Lewis, R. A. Lee, and C. C. Reading, ''Imaging-guided radiofrequency ablation of solid renal tumors,'' AJR, Am. J. Roentgenol. **180**, 1509–1513 (2003).
[25] C. H. Cha, F. T. Lee, Jr., J. M. Gurney, B. K. Markhardt, T. F. Warner, F. Kelcz, and D. M. Mahvi, ''CT versus sonography for monitoring radiofrequency ablation in a porcine liver,'' AJR, Am. J. Roentgenol. **175**, 705–711 (2000).
[26] S. S. Raman, D. S. Lu, D. J. Vodopich, J. Sayre, and C. Lassman, ''Creation of radiofrequency lesions in a porcine model: correlation with sonography, CT, and histopathology,'' AJR, Am. J. Roentgenol. **175**, 1253–1258 (2000).
[27] M. Morimoto, K. Sugimori, K. Shirato, A. Kokawa, N. Tomita, T. Saito, N. Tanaka, A. Nozawa, M. Hara, H. Sekihara, H. Shimada, T. Imada, and K. Tanaka, ''Treatment of hepatocellular carcinoma with radiofrequency ablation: radiologic-histologic correlation during follow-up periods,'' Hepatology **35**, 1467–1475 (2002).
[28] S. N. Goldberg, G. S. Gazelle, C. C. Compton, P. R. Mueller, and K. K. Tanabe, ''Treatment of intrahepatic malignancy with radiofrequency ablation: radiologic-pathologic correlation,'' Cancer **88**, 2452–2463 (2000).
[29] E. Berber, A. Foroutani, A. M. Garland, S. J. Rogers, K. L. Engle, T. L. Ryan, and A. E. Siperstein, ''Use of CT Hounsfield unit density to identify ablated tumor after laparoscopic radiofrequency ablation of hepatic tumors,'' Surg. Endosc. **14**, 799–804 (2000).
[30] P. F. Hahn, G. S. Gazelle, D. Y. Jiang, C. C. Compton, S. N. Goldberg, and P. R. Mueller, ''Liver tumor ablation: real-time monitoring with dynamic CT,'' Acad. Radiol. **4**, 634–638 (1997).
[31] S. S. Chen and J. D. Humphrey, ''Heat-induced changes in the mechanics of a collagenous tissue: pseudoelastic behavior at 37 degrees C,'' J. Biomech. **31**, 211–216 (1998).
[32] J. Ophir, I. Cespedes, H. Ponnekanti, Y. Yazdi, and X. Li, ''Elastography: a quantitative method for imaging the elasticity of biological tissues,'' Ultrason. Imaging **13**, 111–134 (1991).
[33] T. Varghese, J. Ophir, E. Konofagou, F. Kallel, and R. Righetti, ''Tradeoffs in elastographic imaging,'' Ultrason. Imaging **23**, 216–248 (2001).
[34] M. O'Donnell, A. R. Skovoroda, B. M. Shapo, and S. Y. Emelianov, ''Internal displacement and strain imaging using ultrasonic speckle tracking,'' IEEE Trans. Ultrason. Ferroelectr. Freq. Control **41**, 314–325 (1994).
[35] T. A. Krouskop, D. R. Dougherty, and F. S. Vinson, ''A pulsed Doppler ultrasonic system for making noninvasive measurements of the mechanical properties of soft tissue,'' J. Rehabil. Res. Dev. **24**, 1–8 (1987).
[36] R. M. Lerner, S. R. Huang, and K. J. Parker, '''Sonoelasticity' images derived from ultrasound signals in mechanically vibrated tissues,'' Ultrasound Med. Biol. **16**, 231–239 (1990).
[37] L. Sandrin, M. Tanter, S. Catheline, and M. Fink, ''Shear modulus imag-

ing with 2-D transient elastography,'' IEEE Trans. Ultrason. Ferroelectr. Freq. Control **49**, 426–435 (2002).
[38] K. Nightingale, M. S. Soo, R. Nightingale, and G. Trahey, ''Acoustic radiation force impulse imaging: in vivo demonstration of clinical feasibility,'' Ultrasound Med. Biol. **28**, 227–235 (2002).
[39] M. Fatemi and J. F. Greenleaf, ''Application of radiation force in noncontact measurement of the elastic parameters,'' Ultrason. Imaging **21**, 147–154 (1999).
[40] A. Pesavento, A. Lorenz, S. Siebers, and H. Ermert, ''New real-time strain imaging concepts using diagnostic ultrasound,'' Phys. Med. Biol. **45**, 1423–1435 (2000).
[41] T. J. Hall, Y. Zhu, and C. S. Spalding, ''*In vivo* real-time freehand palpation imaging,'' Ultrasound Med. Biol. **29**, 427–435 (2003).
[42] F. Kallel, J. Ophir, K. Magee, and T. Krouskop, ''Elastographic imaging of low-contrast elastic modulus distributions in tissue,'' Ultrasound Med. Biol. **24**, 409–425 (1998).
[43] R. J. Stafford, F. Kallel, R. E. Price, D. M. Cromeens, T. A. Krouskop, J. D. Hazle, and J. Ophir, ''Elastographic imaging of thermal lesions in soft tissue: a preliminary study in vitro,'' Ultrasound Med. Biol. **24**, 1449–1458 (1998).
[44] F. Kallel, R. J. Stafford, R. E. Price, R. Righetti, J. Ophir, and J. D. Hazle, ''The feasibility of elastographic visualization of HIFU-induced thermal lesions in soft tissues. Image-guided high-intensity focused ultrasound,'' Ultrasound Med. Biol. **25**, 641–647 (1999).
[45] R. Righetti, F. Kallel, R. J. Stafford, R. E. Price, T. A. Krouskop, J. D. Hazle, and J. Ophir, ''Elastographic characterization of HIFU-induced lesions in canine livers,'' Ultrasound Med. Biol. **25**, 1099–1113 (1999).
[46] R. Souchon, O. Rouviere, A. Gelet, V. Detti, S. Srinivasan, J. Ophir, and J. Y. Chapelon, ''Visualisation of HIFU lesions using elastography of the human prostate in vivo: preliminary results,'' Ultrasound Med. Biol. **29**, 1007–1015 (2003).
[47] T. Varghese, J. A. Zagzebski, and F. T. Lee, Jr., ''Elastographic imaging of thermal lesions in the liver in vivo following radiofrequency ablation: preliminary results,'' Ultrasound Med. Biol. **28**, 1467–1473 (2002).
[48] T. Varghese, U. Techavipoo, W. Liu, J. A. Zagzebski, Q. Chen, G. Frank, and F. T. Lee, Jr., ''Elastographic measurement of the area and volume of thermal lesions resulting from radiofrequency ablation: pathologic correlation,'' AJR, Am. J. Roentgenol. **181**, 701–707 (2003).
[49] S. Srinivasan, R. Righetti, and J. Ophir, ''Trade-offs between the axial resolution and the signal-to-noise ratio in elastography,'' Ultrasound Med. Biol. **29**, 847–866 (2003).
[50] F. Kallel and J. Ophir, ''A least-squares strain estimator for elastography,'' Ultrason. Imaging **19**, 195–208 (1997).
[51] T. Varghese, J. Ophir, and I. Cespedes, ''Noise reduction in elastograms using temporal stretching with multicompression averaging,'' Ultrasound Med. Biol. **22**, 1043–1052 (1996).
[52] R. C. Gonzalez and R. E. Woods, in *Digital Image Processing*, 2nd ed. (Pearson Education, Inc., 2002), p. 235.
[53] S. N. Goldberg, G. S. Gazelle, L. Solbiati, T. Livraghi, K. K. Tanabe, P. F. Hahn, and P. R. Mueller, ''Ablation of liver tumors using percutaneous RF therapy,'' AJR, Am. J. Roentgenol. **170**, 1023–1028 (1998).
[54] S. Thomsen, ''Pathologic analysis of photothermal and photomechanical effects of laser-tissue interactions,'' Photochem. Photobiol. **53**, 825–835 (1991).
[55] D. E. Dupuy and S. N. Goldberg, ''Image-guided radiofrequency tumor ablation: challenges and opportunities—part II,'' J. Vasc. Interv. Radiol. **12**, 1135–1148 (2001).